Fast outflows in compact radio sources: evidence for AGN-induced feedback in the early stages of radio source evolution

J. Holt,[1][*][†] C. N. Tadhunter[1] and R. Morganti[2]

[1]*Department of Physics and Astronomy, University of Sheffield, Sheffield S3 7RH*
[2]*Netherlands Foundation for Research in Astronomy, Postbus 2, 7990 AA Dwingeloo, the Netherlands*

ABSTRACT

We present intermediate-resolution, wide-wavelength coverage spectra for a complete sample of 14 compact radio sources taken with the aim of investigating the impact of the nuclear activity on the circumnuclear interstellar medium (ISM) in the early stages of radio source evolution. We observe spatially extended line emission (up to $\sim$20 kpc) in the majority of sources which is consistent with a quiescent halo. In the nuclear apertures we observe broad, highly complex emission-line profiles. Multiple Gaussian modelling of the [O III]λ5007 line reveals between two and four components which can have velocity widths [full width at half-maximum (FWHM)] and blueshifts relative to the halo of up to $\sim$2000 km s^{-1}. We interpret these broad, blueshifted components as material in outflow and discuss the kinematical evidence for jet-driven outflows as previously proposed for PKS 1549$-$79 and PKS 1345$+$12. Comparisons with samples in the literature show that compact radio sources harbour more extreme nuclear kinematics than their extended counterparts, a trend seen within our sample with larger velocities in the smaller sources. The observed velocities are also likely to be influenced by source orientation with respect to the observer's line of sight. Nine sources have associated H I absorption. In common with the optical emission-line gas, the H I profiles are often highly complex with the majority of the detected components significantly blueshifted, tracing outflows in the neutral gas. The sample has been tested for stratification in the ISM (FWHM/ionization potential/critical density) as suggested by Holt, Tadhunter & Morganti for PKS 1345$+$12 but we find no significant trends within the sample using a Spearman rank analysis. This study supports the idea that compact radio sources are young radio-loud active galactic nuclei observed during the early stages of their evolution and currently shedding their natal cocoons through extreme circumnuclear outflows.

Key words: ISM: jets and outflows – ISM: kinematics and dynamics – galaxies: active – galaxies: ISM – galaxies: kinematics and dynamics.

1 INTRODUCTION

We currently know little about the early evolution of powerful extragalactic radio sources, in particular, how the presence of a radio-loud active galactic nucleus (AGN) influences the evolution of the host galaxy, and how the interstellar medium (ISM) affects the expansion of the radio jets. Recent developments in both observation and theory have shown the importance of AGN feedback in galaxy evolution. For example, there exist close correlations between the mass of the central black hole and the properties of the galaxy bulge (e.g. Ferrarese & Merritt 2000; Gebhardt et al. 2000; Tremaine et al. 2002; Marconi & Hunt 2003). Theoretical analyses by, for example, Silk & Rees (1998) and Fabian (1999), and more recently, simulations by, for example, Di Matteo, Springel & Hernquist (2005) and Hopkins et al. (2005), describe how, after relocating to the centre of the galaxy remnant after a merger (Heckman et al. 1986), the supermassive black hole grows through accretion, becomes active (a protoquasar) and then sheds its enshrouding cocoon (deposited by the merger) through outflows driven by powerful quasar winds (Balsara & Krolick 1993). With time, the central regions will be cleared of fuel, starving both the central AGN and any star forming regions in the bulge and activity will cease.

Clearly, understanding AGN-induced feedback is of vital importance for understanding the evolution of both AGN and their host galaxies. However, there remain many uncertainties in the models

[*]E-mail: jholt@strw.leidenuniv.nl
[†]Present address: Leiden Observatory, PO Box 9513, 2300 RA Leiden, The Netherlands.

due to a lack of observational evidence, and feedback is often inserted as a 'black box'. Whilst the models described above provide a good theoretical description of the shedding of the natal cocoon during the early evolutionary stages, these scenarios often *assume* that the feedback is dominated by quasar-induced winds. Whilst this may be true for radio-quiet AGN, in radio-loud AGN, the expanding radio jets may also provide a significant contribution to the overall feedback of the AGN through jet-induced outflows (e.g. Bicknell et al. 1997), particularly during the early stages of the radio source evolution when the radio jets are still on the same scales as the natal cocoon. Such a contribution on small scales should not be surprising given the increasing support for significant feedback from extended radio sources, for example, in the quenching of cooling flows in massive haloes (e.g. Best et al. 2006; Bower et al. 2006; Croton et al. 2006).

With this in mind, compact radio sources, comprising the gigahertz-peaked spectrum radio sources (GPS: $D < 1$ kpc) and the larger compact steep spectrum radio sources (CSS: $D < 15$ kpc), form a large proportion of the bright (centimetre-wavelength-selected) radio source population ($\sim$40 per cent; e.g. O'Dea 1998) particularly suited to studying AGN-induced feedback. First, GPS and CSS sources are currently believed to be compact due to evolutionary stage (Fanti et al. 1995) with estimates of dynamical and radio spectral ages of $t_{dyn} \sim 10^2$– 10^3 yr (e.g. Owsianik, Conway & Polatidis 1998; Tschager et al. 2000) and $t_{sp} < 10^4$ yr (e.g. Murgia et al. 1999), respectively. This is in preference to the frustration scenario in which the ISM is so dense that the radio jets cannot escape, and the radio source remains confined and frustrated for its entire lifetime (van Breugel 1984). Secondly, the small-scale radio jets will be on the same scales as the natal cocoon of gas and dust and so will readily interact with it. Finally, radio-loud sources contain all potential outflow driving mechanisms (quasar-induced winds, radio jets and starburst-driven superwinds) and so are the only objects in which the relative importance of the different effects can be assessed in individual objects (e.g. Batcheldor et al. 2007).

The most direct way to probe the kinematics and physical conditions of the nuclear gas is through high-quality optical spectroscopy. However, to date, much of the work on compact radio sources has either concentrated on the radio wavelength region or has relied on low signal-to-noise ratio (S/N) optical spectra. Despite this, an early optical spectroscopic study of a large sample of compact radio sources suggested evidence for non-gravitational motions (indicative of flows of gas) in the form of highly broadened emission-line profiles which are often asymmetric with blue wings (Gelderman & Whittle 1994). However, the potential differences between the spectra of compact and extended sources were not quantified in this early study.

With new, deeper spectra, it becomes clear that the unusually broad nuclear emission lines are due to highly complex emission-line profiles requiring multiple Gaussians to model them. The first concrete evidence for fast outflows in the optical emission-line gas in a compact radio source was reported by Tadhunter et al. (2001) in the southern compact flat spectrum radio source PKS 1549−79. From their low-resolution optical spectra, the high-ionization emission lines (e.g. [O III]) were both broader [full width at half-maximum (FWHM) $\sim$ 1350 km s^{-1} compared to $\sim$650 km s^{-1}] and *blueshifted* by $\sim$600 km s^{-1} with respect to the low-ionization lines (e.g. [O II]). Recent higher resolution follow up on this source has shown that the outflowing component is present in all lines with a velocity of 679 ± 20 km s^{-1} (Holt et al. 2006, hereafter H06). Similarly, Holt, Tadhunter & Morganti (2003) (hereafter H03) reported a much more extreme outflow (up to 2000 km s^{-1}) in the GPS source PKS

1345+12. In both sources, the outflows are believed to be driven by the small-scale radio jets expanding through dense circumnuclear cocoons of gas and dust (see e.g. fig. 2 in Tadhunter et al. 2001 and fig. 4 in H03). A recent high-resolution optical and radio imaging study [*Hubble Space Telescope* (*HST*) and very long baseline interferometry (VLBI)] was able to confidently rule out large-scale starbursts driven winds, but failed to distinguish between jet-driven outflows and AGN-induced winds (Batcheldor et al. 2007). However, previous *HST* imaging studies of compact radio sources have suggested evidence for an alignment effect on small scales in some CSS sources (de Vries et al. 1997, 1999; Axon et al. 2000) which would support the jet-driven outflows scenario. For PKS 1345+12, due to the differences in velocity width between the emission-line components in different lines, H03 suggested a stratified ISM which may be the result of gradients in density and/or ionization potential across the circumnuclear ISM.

Hence, we have obtained intermediate-resolution (4–6 Å[1]) optical spectra with good S/N over a large spectral range, with the WHT, NTT and VLT, in order to search for such outflows in a complete sample of 14 compact radio sources. In this paper, the first of two, we present the kinematical data for the whole sample in order to search for the signatures of outflows in the nuclear emission-line gas. In Sections 2 and 3, we describe the sample selection, observations and data reduction procedure. In Section 4, we model the emission lines, both in the extended halo (to determine the rest frame of each system) and in the nucleus (to search for outflows). Our data are of sufficient resolution to model the lines with multiple Gaussian components. In addition, in Section 5 we have modelled the lines with single Gaussians to allow comparisons between the sample presented here and other samples (compact and extended) in the literature, and to investigate the possibility of density and/or ionization gradients in the ISM in some sources. In this paper we concentrate on the emission-line kinematics and the ionization of the emission-line gas will be discussed in a second paper.

Throughout this paper, we assume the following cosmology: $H_0 = 71$ km s^{-1}, $\Omega_0 = 0.27$ and $\Omega_\Lambda = 0.73$.

2 SAMPLE SELECTION

Our complete sample comprises 14 compact radio sources split across the Northern and Southern hemispheres. In the north, we have observed a complete sample of five sources (three CSS, two GPS with $z < 0.4$, $12^h < $ RA $ < 18^h$ and $\delta > 15°$) from the subset of compact radio sources in the 3rd and 4th Cambridge Radio Catalogues (3C and 4C, respectively, at 178 MHz) listed in Table 1 in the O'Dea (1998) review, which is a master list of the CSS sample from Fanti et al. (1990) and the GPS sample from Stanghellini et al. (1990, 1996). A further seven sources (five CSS, one GPS, one compact flat spectrum) form a complete redshift ($z < 0.7$) and RA ($12^h < $ RA $ < 5^h$) limited subset of the 2 Jy sample of Tadhunter et al. (1993), which in turn is a subset ($z < 0.7$, $\delta < + 10°$) of the 2 Jy Wall & Peacock (1985) radio survey at 2.7 GHz. We have also observed a further two radio sources (3C 213.1 and 3C 459) which are classified as compact core radio sources. Such sources have both extended radio structure (jets and lobes which are often disconnected from the radio core) and a second, compact radio structure (complete with lobes), which may be misaligned from the large-scale source. Whilst the larger-scale structures are consistent

---

[1] This corresponds to $\sim$200–300 km s^{-1}, dependent on redshift, for [O III]5007 Å for the objects in our sample.

Table 1. Properties of the sample: (1) radio source; (2) optical ID where G = galaxy, Q = QSO; (3) radio source type where CSS = compact steep spectrum, GPS = gigahertz-peaked spectrum, CF = compact flat spectrum and CC = compact core; (4) redshift $\star$ redshifts from the literature, for the accurate redshifts derived in this study, see Table 5; (5) radio spectral index where $F_\nu \propto \nu^{-\alpha}$ and for $\alpha_{2.7\,\mathrm{GHz}}^{5\,\mathrm{GHz}}$ (for all but 3C 213.1, 3C 277.1 and 3C 303.1, these are taken from Wall & Peacock 1985; for the remaining three sources α is calculated from the flux densities presented in Kellermann, Pauliny-Toth & Williams 1969); (6) radio luminosity at 5GHz; (7) H I 21-cm absorption velocity (km s^{-1}); (8) H I 21-cm absorption FWHM (km s^{-1}); (9) angular size of radio source in arcseconds; (10) projected linear size of radio source in kiloparsecs; (11) radio axis PA.

Object	ID	Type	$z^\star$	α	Radio luminosity log $P_{5\,\mathrm{GHz}}$ (W Hz^{-1})	H I 21-cm absorption V_{helio} (km s^{-1})	FWHM (km s^{-1})	Angular size (arcsec)	Linear size (kpc)	Radio PA (°)
(1)	(2)	(3)	(4)	(5)	(6)	(7)	(8)	(9)	(10)	(11)
3C 213.1	G	CC	0.195	0.30	26.41	0.193 95	115	6.0[b]	19.1[b]	−61
								40[c]	128[c]	−20
3C 268.3	G	CSS	0.371	0.88	27.04	0.371 86	101	1.36	6.9	−15
						0.372 27	19			
3C 277.1	Q	CSS	0.320	0.61	26.86	–	–	1.67	7.7	−49
4C 32.44	G	GPS	0.369	0.60	27.30	0.368 43	229	0.06	0.31	−50
PKS 1345+12	G	GPS	0.122	0.44	26.69	0.121 84	150	0.15	0.33	160
3C 303.1	G	CSS	0.267	1.08	26.43	–	–	1.80	7.3	−47
PKS 0023−26	G	CSS	0.322	0.7	27.43	0.318 90	126	0.68	3.2	−34
						0.321 42	39			
PKS 0252−71	G	CSS	0.566	1.14	27.55	–	–	0.24	1.6	7
PKS 1306−09	G	CSS	0.464	0.65	27.39	0.464 92[d]	350[d]	0.46	15.7	−41
PKS 1549−79	G	CF	0.152	0.18	27.00	0.152 24		0.12	0.3	90
PKS 1814−63	G	CSS[a]	0.063	0.91	26.54	0.064 50		0.41	0.5	−20
PKS 1934−63	G	GPS[a]	0.183	0.88	27.31	0.182 82	18	0.70	2.1	89
PKS 2135−20	G	CSS	0.635	0.82	27.58	–	–	0.25	1.7	52
PKS 2314+03	G	CC	0.220	0.97	27.65	0.218 50[e]	∼400	0.20[b]	0.7[b]	95
						0.219 14[f]	130	10.00[c]	35.2[c]	
						0.218 37[g]	71			
						0.218 39[g]	121			
						0.219 63[g]	164			

[a]Taken from the literature and may be inconsistent with the sizes in column (10). [b]Compact core component in 3C 213.1 and 3C 459. [c]Extended radio source component in 3C 213.1 and 3C 459. [d]Tentative H I detection with optical depth, $\tau = 0.003$ (Morganti, private communication) where the central velocity is assumed to be the midpoint of the entire absorption profile. For 3C 459 the different H I results are: [e]Morganti et al. (2001), [f]Vermeulen et al. (2003) and [g]Gupta et al. (2006).

with old, evolved radio sources, the inner, compact structures may represent a younger, more recently triggered active phase, and so these sources can be studied in conjunction with a sample of compact radio sources.

The whole sample has a radio power range of $26 < \log P_{5\,\mathrm{GHz}}$(W Hz^{-1}) < 28. Details of the sample are presented in Table 1. Hence, the total sample includes eight CSS, three GPS, one compact flat spectrum source and two compact core radio sources. The sample also includes both galaxy (13) and quasar (1) host morphologies.

The subsamples were chosen to fulfil the following criteria: (i) redshifts low enough to include [O III]λ5007 in the spectra and similar for the subsamples; (ii) right ascension and declination ranges to be observed during the allocated runs and (iii) the samples were derived from well-studied samples (2 Jy, 3C and 4C) to enable good comparisons between compact and extended sources.

3 OBSERVATIONS, DATA REDUCTION AND ANALYSIS TECHNIQUES

Long-slit optical spectroscopic observations of the full sample were obtained during two observing runs. The northern sample was observed on 2001 May 12–14 with ISIS, the dual arm spectrograph on the 4.2-m William Herschel Telescope on La Palma. In the red,

the TEK4 CCD was used with the R316R grating with 1×1 binning and two central wavelengths (∼6950 and 8450 Å, dependent on object). The resulting wavelength calibration accuracies, calculated using the standard error on the mean deviation of the night sky emission-line wavelengths from published values Osterbrock et al. 1996, were 0.06–0.11 Å (∼6950 Å) and 0.10–0.53 Å (∼8450 Å). The spectral resolutions, calculated using the widths of the night sky emission lines, were 3.3–3.7 ± 0.1 Å (∼6950 Å) and 3.8–4.1 ± 0.1 Å (∼8450 Å). In the blue, the EEV12 CCD was used with the R300B grating with 2×2 binning. The wavelength calibration accuracy was 0.1–0.2 Å with a spectral resolution of 4.3–4.8 ± 0.2 Å. The spatial scale was 0.36 arcsec pixel^{-1}. Further details, including the instrumental set-ups and the useful wavelength ranges of the spectra are summarized in Table 2.

The southern sample was observed on 2002 July 12–13 using the EMMI spectrograph on the ESO New Technology Telescope (NTT) on La Silla, Chile in RILD mode. The MIT/LL CCD was used with grisms #4, #5 and #6 to obtain spectra with central wavelengths 7935, 5385 and 7223 Å with 2×2 binning. The wavelength calibration accuracies were 0.24 Å (7935 Å), 0.06–0.15 Å (5385 Å) and 0.10–0.17 Å (7223 Å) with spectral resolutions of 14 ± 1 Å (7935 Å), 5.6 ± 0.1 Å (5385 Å) and 4.3–6.7 ± 0.1 Å (7223 Å). The spatial scale was 0.33 arcsec pixel^{-1}. Again, further details are presented in Table 2.

Table 2. Log of observations. Column (1) denotes the arm/wavelength range of the spectrograph. Column (8) is the instrumental seeing († indicates seeing measured using the object continuum – for all other sources, a star on the chip was used). Note, the values quoted in column (8) represent upper limits on the true seeing as (i) where the seeing was measured using the target galaxy, these measurements may be affected by the extended galaxy haloes i.e. they are not stellar and (ii) the measurements based on the profiles of stars along the slit only provide a good seeing estimate if the slit passes through the centres of the stellar image, otherwise the FWHM (and therefore seeing) will be overestimated. Column 9 gives the width of the extracted nuclear aperture in arcseconds, centred on the centroid of the nuclear continuum emission (quoted once per object in the table but the same aperture was used for both red and blue spectral ranges) and column 10 denotes the photometric conditions (p = photometric, v = variable transparency). ⋆ denotes spectra taken aligned within 10° of the radio source PA.

Date	Object	'Arm'	Exposure	Slit PA	Slit Width	λ range	Seeing	Nuclear aperture	Notes
			(s)	(°)	(arcsec)	(Å)	(arcsec)	(arcsec)	
(1)	(2)	(3)	(4)	(5)	(6)	(7)	(8)	(9)	(10)
WHT/ISIS observations									
14/05/2001	3C 213.1	R	3 × 1200	80⋆	1.3	7700–9200	1.5 ± 0.1†	2.5	v
		B	3 × 1200	80⋆	1.3	3300–6800	1.8 ± 0.1†		v
13/05/2001	3C 268.3	R	2 × 1200	155⋆	1.3	7850–9350	1.4 ± 0.3†	2.2	p
		R	3 × 1200	155⋆	1.3	6200–7700	1.9 ± 0.2†		p
		B	5 × 1200	155⋆	1.3	3700–6800	2.3 ± 0.2†		p
13/05/2001	3C 277.1	R	1 × 1200	129⋆	1.3	7850–9350	0.9 ± 0.1†	1.8	p
		R	2 × 1200	129⋆	1.3	6200–7700	0.9 ± 0.1†		p
		B	3 × 1200	129⋆	1.3	3700–6800	1.4 ± 0.1†		p
14/05/2001	4C 32.44	R	3 × 1200	105	1.3	7700–9200	1.5 ± 0.2†	2.5	v
		R	3 × 1200	105	1.3	6200–7700	1.4 ± 0.2†		v
14/05/2001		B	3 × 1200	105	1.3	3300–6800	1.9 ± 0.2†		v
12/05/2001	PKS 1345+12	R	1 × 900	104	1.3	6200–7700	1.3 ± 0.2	2.2	p
	(4C 12.50)	B	1 × 900	104	1.3	3300–6800	1.3 ± 0.2		p
		R	3 × 1200	160⋆	1.3	6200–7700	1.3 ± 0.2		p
		B	3 × 1200	160⋆	1.3	3300–6800	1.3 ± 0.2		p
14/05/2001	PKS 1345+12	R	3 × 1200	230	1.3	6200–7700	1.7 ± 0.2	2.2	v
		B	3 × 1200	230	1.3	3300–6800	1.7 ± 0.2		v
12/05/2001	3C 303.1	R	5 × 1200	130⋆	1.3	7700–9200	1.8 ± 0.1†	2.5	p
		B	5 × 1200	130⋆	1.3	3300–6800	1.8 ± 0.1†		p
NTT/EMMI observations									
13/07/2002	PKS 0023−26	B	3 × 1200	−105	1.5	3700–7050	2.5 ± 0.2†	2.0	p
		R	2 × 1200	−105	1.5	4400–114 00	2.3 ± 0.2†		p
13/07/2002	PKS 0252−71	R	2 × 1200	135⋆	1.5	5700–8700	1.6 ± 0.1	1.7	p
		B	2 × 1200	135⋆	1.5	3700–7050	1.5 ± 0.1		p
13/07/2002	PKS 1306−09	R	3 × 1200	135	1.0	5700–8700	1.7 ± 0.2†	2.3	p
		B	3 × 1200	135	1.0	3700–7050	1.8 ± 0.2†		p
12/07/2002	PKS 1549−79	R	3 × 1200	−5	1.0	5700–8700	1.9 ± 0.1		p
		B	3 × 1200	−5	1.0	3700–7050	2.2 ± 0.1		p
		R	2 × 1200	25	1.5	5700–8700	0.8 ± 0.1		p
		B	2 × 1200	25	1.5	3700–7050	0.8 ± 0.1		p
12/07/2002	PKS 1814−63	R	1 × 1200	−72	1.0	5700–8700	1.1 ± 0.2†	1.0	p
		R	1 × 1200	65	1.0	5700–8700	1.3 ± 0.1		p
		B	1 × 1200	65	1.0	3700–7050	1.2 ± 0.1		p
12/07/2002	PKS 1934−63	R	3 × 1200	−20	1.5	5700–8700	1.2 ± 0.1	2.0	p
		B	3 × 1200	-20	1.5	3700–7050	1.2 ± 0.1		p
13/07/2002	PKS 2135−20	R	3 × 1200	−115	1.5	5700–8700	1.4 ± 0.2†	1.7	p
		B	3 × 1200	−115	1.5	3700–7050	1.4 ± 0.2†		p
12/07/2002	3C 459	R	3 × 1200	−175	1.5	5700–8700	1.5 ± 0.2†	1.7	p
	(PKS 2314+03)	B	3 × 1200	−175	1.5	3700–7050	1.5 ± 0.2†		p
		R	1 × 1200	95⋆	1.5	5700–8700	1.5 ± 0.2†		p
VLT/FORS2 observations									
24/09/2003	PKS 1549−79	R	3 × 1200	75	1.3	4950–8250	2.0 ± 0.1	1.5	p
24/09/2003		B	3 × 600	75	1.3	3050–6000	2.1 ± 0.1		p

PKS 1549−79 was also observed with the FORS2 spectrograph on the ESO Very Large Telescope (VLT) on Cerro Paranal, Chile, in 2003 September to improve the S/N of the fainter features and resolve a seeing slit width matching problem in the NTT data. The detailed analysis of the data for PKS 1345+12 and PKS 1549−79 have already been presented in H03, H06 and Rodriguez Zau-

rin et al. (2008). The spatial scale for the VLT observations was 0.25 arcsec pixel^{-1}.

The aim of this project is to search for outflows in the circumnuclear regions using optical spectroscopy with sufficient spectral resolution and S/N to accurately separate and model the different components of the highly broadened and complex emission lines.

In order to include all of the outflowing regions in the slit, and to ensure the spectra were of sufficient resolution, all spectra were taken with a 1.0–1.5 arcsec slit. To reduce the effects of differential atmospheric refraction, all exposures were taken at low airmass (sec $z < 1.1$) and/or with the slit aligned along the parallactic angle. Due to various observational constraints, we have only aligned the slit along the radio axis for approximately half of the sources, and the position angles (PAs) are listed in Table 2. However, as this study is concerned with compact rather than extended radio sources, the feedback effects we are interested in will be confined to the nuclear regions and the misalignment of the slit with the radio axis will not affect our results.

3.1 Data reduction and analysis

The data were reduced in the usual way (bias subtraction, flat-fielding, cosmic ray removal, wavelength calibration, flux calibration) using the standard packages in IRAF. The 2D spectra were also corrected for spatial distortions of the CCD. To reduce wavelength calibration errors due to flexure of the telescope and instrument (ISIS observations), separate arcs were taken at each position on the sky. Such calibrations were not made for EMMI or FORS2 as the reported flexure is small. The calculated wavelength calibration accuracies and spectral resolutions are given above.

Comparison of several spectrophotometric standard stars taken with a wide slit (5 arcsec) throughout each run gave relative flux calibrations accurate to ± 5 per cent. This accuracy was confirmed by good matching in the flux between the red and blue spectra. The only exception was 3C 303.1 and whilst this will pose problems for line ratios, the kinematic information is unaffected. In order to correct the spectra for atmospheric absorption features (e.g. A and B bands at ~ 7600 and ~ 6800 Å, respectively), standard stars were observed with a narrow slit, matched to the slit width used to observe the objects. For the ISIS observations, these were observed at random during the run and the normalized spectra had to be scaled to match the depth of the absorption features. For the NTT and VLT observations, a separate calibration star was observed for each object, close in both position and time to the target observations and so no scaling was required. The spectra of all sources were corrected for Galactic extinction using the $E(B - V)$ values from Schlegel, Finkbeiner & Davis (1998) and the Seaton (1979) extinction law.

The spectra were extracted and analysed using the STARLINK packages FIGARO and DIPSO.

3.2 Continuum subtraction

Prior to emission-line modelling of the nuclear apertures, the continuum was modelled and subtracted for most of the sources. Initially, a nebular continuum was generated and subtracted following Dickson et al. (1995) taking full account of reddening following H03. The remaining continuum was then modelled using a customized IDL minimum χ^2 fitting programme (see e.g. Robinson 2001; Tadhunter et al. 2005; Holt et al. 2007 for details). The modelling program allows up to three separate continuum components – Old (OSP, here set to 12.5 Gyr with no reddening) and Young Stellar Populations (YSP, reddened with $0 < E(B - V) < 1.6$ using Seaton 1979 with age 0.01–5.0 Gyr) taken from Bruzual & Charlot (1993) and an AGN/power-law component. We define the best-fitting model as that with the least number of components required to adequately model both the overall spectral energy distribution (SED) and discrete stellar absorption features (e.g. Ca H&K, Balmer series).

Continuum modelling and subtraction was necessary for the detection and accurate modelling of the broader emission-line components. For completeness, details of the continuum models used for subtraction prior to emission-line modelling are given in Table 3. Note that the continua of several galaxies in this sample have been more recently accurately modelled and we refer readers to the corresponding papers: PKS 1345+12 (Tadhunter et al. 2005; Rodriguez Zaurin et al. 2008); PKS 1549−79 (H06); PKS 0023−26, PKS 1549−79 and PKS 2135−20 (Holt et al. 2007); 3C 213.1 and 3C 459 (Wills et al. 2008).

Table 3. Summary of the continuum modelling results (see also Section 3.2) for the nuclear aperture of all galaxies in the sample. The columns are: (1) object, (2) best-fitting (lowest χ^2_{reduced}) model – OSP (12.5 Gyr) plus YSP (Gyr) + power-law components, (3) percentage (flux) contribution of OSP, (4) percentage (flux) contribution of YSP, (5) $E(B - V)$ value (if any) used to redden the YSP, 6 percentage (flux) contribution of the power-law component, (7) spectral index of the power-law component where $F_\lambda \propto \lambda^\alpha$, (8) minimum reduced χ^2 of the model for the whole SED. The nuclear continuum was not modelled for three galaxies: ⋆ 3C 277.1: pure QSO spectrum; ⋄ PKS 1814−63: continuum is strongly contaminated by a nearby Galactic star which drowns out any continuum information from the galaxy; † 3C 303.1: mismatching between the blue and red arms as the blue arm was observed without a dichroic (due to the position of [O III]$\lambda\lambda4959,5007$). For these three galaxies, see the text for a discussion of alternative techniques. More detailed studies of the stellar populations in some of the radio sources in this sample are presented elsewhere and we refer readers to the following papers: PKS 1345+12 (Tadhunter et al. 2005; Rodriguez Zaurin et al. 2008), PKS 1549−79 (H06), PKS 0023−26 and PKS 2135−20 Holt et al. (2007) and 3C 213.1 and 3C 459 Wills et al. (2008).

Object	Best-fitting model	12.5 Gyr	YSP	$E(B - V)$	Power law	α	$\chi^2_{\text{min.red.}}$
(1)	(2)	(3)	(4)	(5)	(6)	(7)	(8)
3C 213.1	$12.5 + 1.0$	44 ± 2	61 ± 2	0.0	–	–	0.62
3C 268.3	$12.5 + 1.0 + \alpha$	6^{+14}_{-6}	3^{+14}_{-3}	0.0	84^{+7}_{-9}	1.8 ± 0.2	1.22
3C 277.1⋆	–	–	–	–	–	–	–
PKS 1345+12	$12.5 + 0.1 + \alpha$	48^{+8}_{-7}	19^{+12}_{-19}	0.0	19^{+22}_{-17}	$2.86^{+4.08}_{-1.40}$	1.07
4C 32.44	$12.5 + 0.5$	95 ± 3	8 ± 2	0.0	–	–	1.34
3C 303.1†	–	–	–	–	–	–	–
PKS 0023−26	$12.5 + 0.1$	46 ± 16	51 ± 18	1.1	–	–	1.46
PKS 0252−71	$12.5 + 2.0 + \alpha$	2^{+35}_{-2}	57^{+17}_{-39}	0.1	39^{+15}_{-16}	$1.14^{+0.39}_{-0.75}$	1.23
PKS 1306−09	$12.5 + 1.0 + \alpha$	52^{+20}_{-21}	20 ± 20	0.4	31^{+11}_{-13}	$0.85^{+0.50}_{-1.08}$	1.11
PKS 1549−79	$12.5 + 0.1 + \alpha$	34^{+18}_{-14}	39^{+5}_{-9}	0.1	22^{+18}_{-16}	$2.98^{+2.42}_{-1.02}$	0.49
PKS 1814−63⋄	–	–	–	–	–	–	–
PKS 1934−63	$12.5 + \alpha$	85 ± 6	–	–	16 ± 4	$1.56^{+0.28}_{-0.33}$	0.59
PKS 2135−20	$12.5 + 0.1 + \alpha$	16^{+21}_{-16}	49^{+11}_{-12}	0.0	37^{+16}_{-15}	0.66 ± 1.20	0.59
3C 459	$12.5 + 0.05$	34 ± 1	67 ± 1	0.0	–	–	0.43

The continua of three sources were not modelled. 3C 277.1 has a pure quasar continuum (there is no evidence for an underlying stellar continuum), but it could not be reproduced by a simple power law, and so we have not modelled or subtracted the continuum. However, when modelling the emission lines, care was taken to remove the BLR contamination. The radio source PKS 1814−63 lies close to a bright foreground Galactic star and so the spectra are strongly contaminated by light from this star. Fortunately our observations were made during good seeing conditions[2] and we clearly resolve PKS 1814−63 from the star. Whilst it was not possible to model the continuum, for accurate modelling of the broader emission-line components, we have attempted to remove the stellar spectrum. Because the star is point-like, its spectrum will have no significant spatial variation and the star itself could be used for subtraction. Hence, each frame was copied, inverted and then shifted in the spatial direction, so the centroid of the continuum was aligned. The inverted spectrum was then subtracted from the original spectrum to remove the contamination from the continuum emission. Finally, no corrections were made for 3C 303.1 due to the mismatching of the blue and red arm spectra.

3.3 Kinematic component definitions

The emission lines and their components vary significantly in width (FWHM). Hence, for our analysis, we define the following kinematical components for the narrow-line region (NLR) as used in H03:

(i)   narrow: FWHM $< 600\,\mathrm{km\,s^{-1}}$;
(ii) intermediate: $600 < \mathrm{FWHM} < 1400\,\mathrm{km\,s^{-1}}$;
(iii) broad: $1400 < \mathrm{FWHM} < 2000\,\mathrm{km\,s^{-1}}$;
(iv) very broad: FWHM $> 2000\,\mathrm{km\,s^{-1}}$.

4 RESULTS

In this section we discuss the kinematic results derived from 2D optical spectra. Initially, the extended line emission is used to establish the systemic velocities followed by detailed modelling of the emission lines in the nuclear apertures.

4.1 Kinematics of the extended gaseous halo

In order to investigate the impact of the activity on the circumnuclear material, it is first necessary to establish the *exact* redshift of the galaxy rest frame. Many of the objects in the sample show clear evidence for extended emission lines, most notably the [O II]$\lambda\lambda3727$ doublet and [O III]$\lambda5007$, and in some cases Hα $\lambda6562$ (see below). By modelling these, pixel by pixel, across the entire spatial extent, one can determine the radial velocity profile of the host galaxy (see also e.g. H03, H06). All such spatial fitting was done before modelling and subtracting the continuum and the emission lines were fitted using free fits. We define 'free fitting' as when the only constraints used for the emission-line modelling are those set by atomic physics (i.e. the separation, ratio of intensities and velocity widths of line components in a doublet emitted by a single ion). The

radial velocity profiles for all sources are shown in Fig. 1.[3] We have determined the systemic velocities using a variety of techniques.

(i)   Sources with resolved extended emission: Where the line emission line is clearly resolved we have assumed the extended narrow line emission traces the quiescent halo gas as in PKS 1345+12. For two sources (3C 277.1 and PKS 1934−63), the extended gas has settled into what appears to be a smooth rotation curve whilst for the remaining sources, the gas is more similar to that in PKS 1345+12 − consistent with gravitational motions in an elliptical galaxy (velocity amplitude $\leqslant 350\,\mathrm{km\,s^{-1}}$; Tadhunter, Fosbury & Quinn 1989) but not yet completely settled. This technique is the most reliable for determining the systemic velocity and we have used this for most sources in the sample.
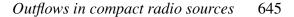
(ii) Sources with two narrow components: In four sources (3C 268.3, 4C 32.44, PKS 0252−71 and PKS 1306−09) we detect two narrow components in the nuclear aperture (for 3C 268.3, and marginally PKS 1306−09, these components are also extended and spatially resolved). Free fitting of the emission lines gives similar but slightly different FWHM. Forcing the two narrow components to have the same FWHM also gives a good fit, and so we assume the two narrow components are emitted by the same mechanism/structure. Hence, the narrow line splitting we observe could represent a rotation curve which is unresolved, or trace a bipolar outflow in the gas. For these sources, we can therefore assume with reasonable confidence that the systemic velocity is located between the two narrow components.

(iii) Other methods: For two sources, we have little confidence in determining the systemic velocity. For PKS 1814−63, the foreground star obscures our view of the galaxy. Using the continuum subtraction technique described in Section 3.2, we have been able to model the extended line emission along two PAs. Along PA 65 the shape of the profile is unclear whilst along PA −72 a more defined shape is observed, which may be consistent with half of the rotation curve. For PKS 2135−20, we are the least certain and have made no attempt to estimate the systemic velocity – the source is unresolved and no narrow components are observed (the narrowest has FWHM $\sim 760\,\mathrm{km\,s^{-1}}$). In addition to the emission-line measurements, we have attempted to measure the stellar absorption lines (e.g. Ca II K and some of the higher order Balmer lines) in a more recently obtained VLT spectrum (see Holt et al. 2007) and estimate a redshift of 0.635 ± 0.004.

Using the above methods, we have confidently determined the systemic velocity in 12 of the 14 sources (3C 213.1, 3C 268.3, 3C 277.1, 4C 32.44, PKS 1345+12, PKS 1549−79, PKS 1934−63, 3C 459 and with some assumptions, 3C 303.1, PKS 0023−26, PKS 1306−09 and PKS 0252−71). Due to the issues discussed above, the velocities for PKS 1814−63 and PKS 2135−20 should be used with caution. Further, for all sources, the velocity amplitude of the narrow component is coincident with gravitational motions in an elliptical galaxy ($\leqslant 350\,\mathrm{km\,s^{-1}}$; Tadhunter et al. 1989).

The derived/assumed systemic velocities are marked on Fig. 1, and it should be noted that zero on the *y*-axis of the velocity profile plots in Fig. 1 does not mark the assumed systemic velocity, which is denoted by the horizontal dashed line. The results are summarized in Table 5. Note that whilst the extended gas was used to

---

[2] Table 2 gives the seeing measured from a star on the 2D spectra whereas the seeing measured using several stars on the acquisition image was 0.8 arcsec.

[3] Note that for some objects the velocity fields are only marginally resolved (see Section 3 and Table 2 for details of the spatial scale and the seeing) and this is why in some of the plots in Fig. 1, the velocities do not appear to vary significantly.
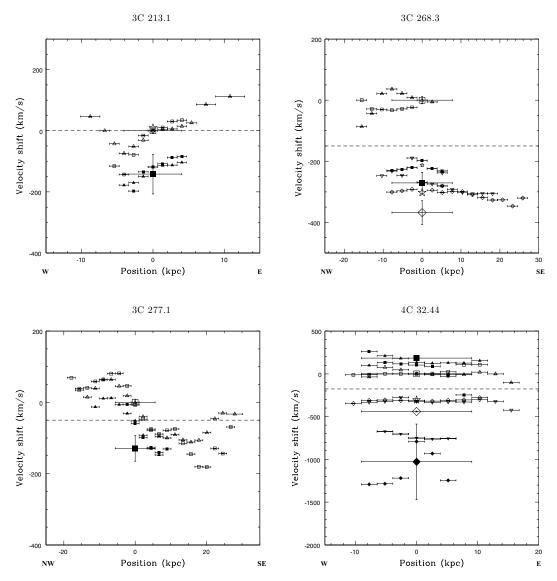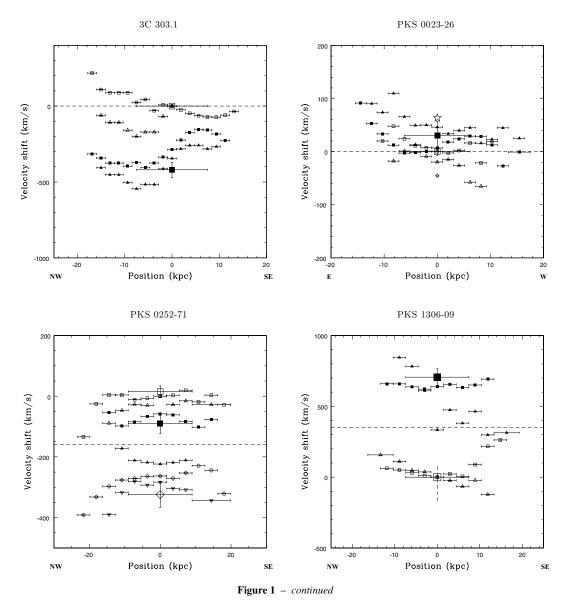
Figure 1. Rest-frame velocity profiles for all sources in the sample. The numerous small points represent the pixel-by-pixel fitting where triangles ($\triangle$, $\triangledown$) are [O II]$\lambda\lambda$3727 and squares/diamonds ($\square$, $\diamond$) are [O III]$\lambda\lambda$4959,5007. In general, open symbols ($\triangle$, $\triangledown$, $\square$, $\diamond$) are narrow components (where two narrow components are present, the second is traced by inverted triangles and diamonds), filled symbols represent the intermediate ($\blacktriangle$,$\blacksquare$) and broad ($\blacktriangledown$,$\blacklozenge$) components. Exceptions are: 4C 32.44 ($\blacktriangle$,$\blacksquare$: broad component; $\blacktriangle$,$\blacklozenge$: very broad component), PKS 1306$-$09 (open and filled points are narrow components), PKS 1814$-$63 ([O III] and Hα emission plotted where $\square$, $\blacksquare$: [O III] and $\diamond$, $\blacklozenge$: Hα), PKS 1934$-$63 & 3C 459: (open: narrow, filled: broad), PKS 2135$-$20 (open: intermediate, filled: broad). Stars (where shown) mark the velocity of the detected H I absorption. Sources to note are: PKS 0023$-$26 (two components, small: narrow, large: broad), PKS 1306$-$09 (vertical dashed line marks the range of velocities over which H I absorption has been tentatively detected, Morganti, private communication), PKS 1814$-$63 (in addition to the deep H I absorption line (star), the range of velocities covered by the broad shallow absorption feature are marked by the vertical dashed line) and 3C 459 (large star: Morganti et al. (2001) detection, large inverted star: Vermeulen et al. (2003) detection, small stars: three components detected by Gupta et al. (2006)). The large symbols ($\square$, $\diamond$, $\blacksquare$, $\blacklozenge$) represent the components of [O III]$\lambda\lambda$4959,5007 detected in the nuclear aperture where the symbols (open/filled etc.) are consistent with the smaller points in the same plot. The large symbols and their horizontal error bars show the position and size of the nuclear aperture. Finally, for 3C 459 (PA 95), two further points mark an extended region of line splitting ([O III]; $\circ$: narrow, $\bullet$: broad) All extended apertures will be discussed in a future paper. The horizontal dashed line in each plot indicates the assumed systemic velocity (derived from [O III]). Note, for PKS 1345+12, this figure includes all three PAs observed and is taken directly from H03. For PKS 1549$-$79, we show the velocity profile along PA $-$5 only, again, taken directly from H06. For more details see H03, H06 and Rodriguez Zaurin et al. (2008). Note, where velocity (vertical) error bars are not clearly seen, the error bars are on the same scale as/smaller than the plotted points.

determine the location of the systemic velocity with respect to the various emission-line components, the redshifts quoted as systemic in Table 5 were derived using measurements of several emission lines (narrow components) in the *nuclear apertures* (as part of the modelling in Section 4.2) rather than based on measurements of [O III] alone.

In addition to the velocities of the extended emission-line components in Fig. 1, the components of the nuclear [O III] lines are shown (see Section 4.2). In the majority of the radial velocity profiles, there is a clear offset in velocities of the broader components between the extended and nuclear apertures of the order of $\sim$100 km s^{-1}. This is most likely due to continuum subtraction

3C 303.1

PKS 0023-26

PKS 0252-71

PKS 1306-09

Figure 1 – *continued*

effects in the nuclear apertures and/or integrating over a larger aperture.

H I 21-cm absorption is detected in 10 of the 14 sources (see Table 6) and the velocities of the detected components are plotted on Fig. 1. In four sources (3C 213.1, 4C 32.44, PKS 1345+12 and PKS 1549−79) at least one component of H I is in agreement with the assumed systemic velocity. However, it is striking that the majority of detected H I components are significantly blueshifted with respect to the optically derived systemic velocities and, in the case of PKS 1345+12 at least, appear to trace the optical outflow. In only two sources is the H I redshifted, consistent with infalling gas (PKS 0023−26 and PKS 1934−63).
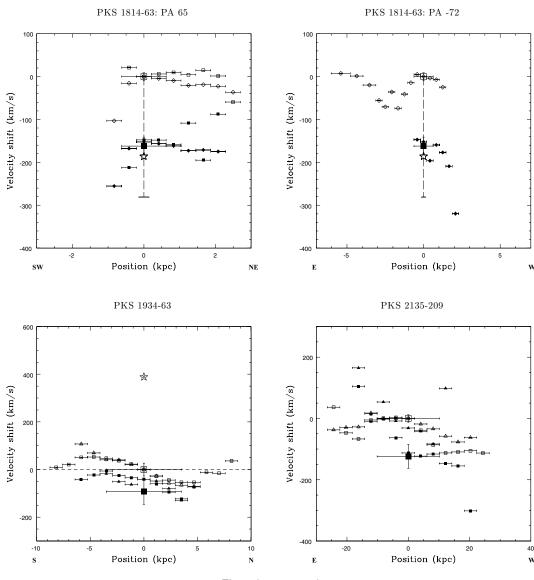
4.2 Emission-line modelling

As discussed in Section 1, the nuclear emission lines in compact radio sources are often broad with asymmetric profiles requiring multiple Gaussian components to model them. In Section 4.1, we identified the rest frame for each source. Here, after subtracting the continuum, we model all strong emission lines in the nucleus

to search for outflows. In addition to multiple Gaussian fitting following H03, we present the results of single Gaussian fitting and asymmetry indices. These latter two steps will allow us to make comparisons between our data and previous work.

4.2.1 Multiple Gaussian modelling

The nuclear emission lines in compact radio sources are often broad with asymmetric profiles. Hence, single Gaussians are unable to adequately model the line profiles and multiple components are required. As an example, Fig. 2 shows how fitting 1, 2 and 3 Gaussians to [O III]λλ4959,5007 in the nucleus of PKS 0252−71 affects the quality of the overall fit.

When modelling the emission-line spectra of AGN, it is common to start with the brightest emission lines, e.g. the [O III]λλ4959,5007 doublet (e.g. Villar-Martín et al. 1999). The [O III] lines were fitted using three constraints in accordance with atomic physics: the flux ratio between [O III]λ4959 and [O III]λ5007 was set at 2.99:1 (based on the transition probabilities; Osterbrock 1989); the widths of the corresponding components of each line were forced to be equal;

PKS 1814-63: PA 65

PKS 1814-63: PA -72

PKS 1934-63

PKS 2135-209

Figure 1 – *continued*

and the shifts between the corresponding components of each line were fixed to be 48.0 Å. Note that the fitting program used can only work with a wavelength difference and not a ratio of wavelengths. However, we find the incurred error is smaller than our estimated uncertainty.

Following the technique of H03, we have modelled the [O III] lines using the *minimum* number of Gaussians required to give a good fit.[4] Hence, for all sources in the sample the fits to [O III] required between 2 and 4 Gaussian components to model the doublet well. The best-fitting models are presented in Fig. 3 and the line data (velocity widths,[5] relative shifts) are presented in Table 4. The errors quoted

in Table 4 are a combination of the measurement errors (taken from DIPSO) and an estimation of the expected errors based on the spectral resolution of the spectra. Typically, for the weaker and/or broader components, the DIPSO error is representative of the true error on the result. For the stronger and/or narrower components, the DIPSO error is very small ($\ll$1 per cent) and is not a good indicator of the true errors. For these sources, we have estimated a percentage error based on the spectral resolution and S/N of the data. This is typically of the order of few to 10 per cent. In addition, the velocities of the nuclear [O III] lines are overplotted on the radial velocity profiles in Fig. 1.

From Fig. 3 it is clear that a number of sources show extreme linewidths and shifts, particularly PKS 1345+12, 4C 32.44, PKS 1549−79 and 3C 459. It is interesting to note that these sources account for four out of the five smallest sources in the sample, each having a radio source with linear size <1 kpc.[6] For the fifth

[4] Note that we define a 'good fit' to the emission lines as that which, by eye, has acceptably low residuals and fits all of the major features (peaks/wings etc.) of the overall line profile well.
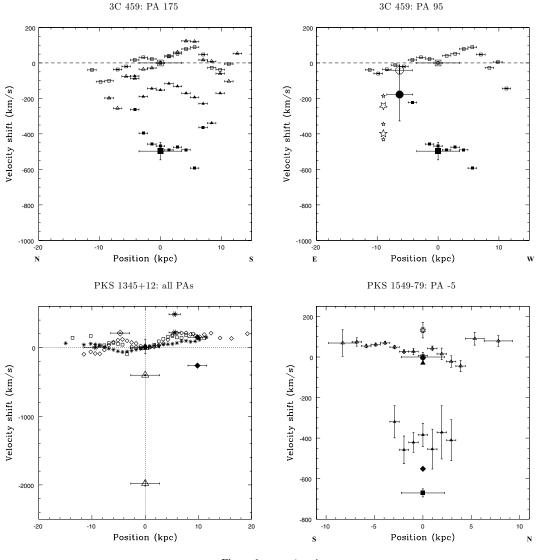
[5] Linewidths are corrected for instrumental width using the equation: $FWHM_c = \sqrt{FWHM_m^2 - IW^2}$ where $FWHM_c$ is the corrected FWHM of the line (in Å), $FWHM_m$ is the measured FWHM of the line (in Å) and IW is the instrumental width or spectral resolution, calculated using the measured widths of the night sky lines.

[6] Note, for 3C 459, whilst the overall radio source is highly extended the compact core is consistent with the other compact radio sources in the sample.

Figure 1 – *continued*

source in this group, PKS 1814−63, non-detection of broader, more blueshifted components may be real although difficulties in subtracting the continuum due to the presence of a foreground star may also influence the result.

When modelling the emission lines in AGN, it is often assumed that one model will reproduce *all* emission lines. This technique has been particularly successful in studies of jet–cloud interactions in powerful radio galaxies (e.g. Villar-Martín et al. 1999; Taylor, Tadhunter & Robinson 2003). Hence, after modelling [O III] in nuclear aperture of each source, we attempted to model the other nuclear emission lines with the same components and the same velocity widths and shifts as the corresponding [O III] model, hereafter the [O III] model.

As well as the constraints from the [O III] model, some emission-line doublets required further constraints in accordance with atomic physics: the shift between the corresponding components of each line in all doublets (e.g. [Ne III]$\lambda\lambda$3868,3968, [Ne V]$\lambda\lambda$3346,3425, [N II]$\lambda\lambda$6548,6583, [O I]$\lambda\lambda$6300,6363 and [S II]$\lambda\lambda$6716,6731) were set and for some doublets (e.g. [Ne III]$\lambda\lambda$3868,3968, [Ne V]$\lambda\lambda$3346,3425, [N II]$\lambda\lambda$6548,6583, and [O I]$\lambda\lambda$6300,6363) the flux ratios were set based on the transition probabilities. For

[S II]$\lambda\lambda$6716,6731, the flux ratio was required to be within the range 0.44 < [S II]6716/6731 < 1.42, the ratios corresponding to the high and low density limits, respectively.

With the exception of PKS 1345+12 and PKS 1934−63, one model (the '[O III] model') fitted the other emission lines well. For PKS 1345+12, only the narrow component was consistently found in all lines whilst in PKS 1934−63, none of the emission-line components was consistent in all lines. However, it should be noted that, due to the complexity of the emission-line profiles in all sources, it was often necessary to force the position of the narrow component to be at the systemic redshift to obtain a good fit to the lines with the [O III] model. Further, in sources where two narrow components are detected, whilst free fitting gave different FWHM for the two components, it was also possible to obtain a good overall fit forcing the two narrow components to have equal FWHM (e.g. 3C 268.3, 4C 32.44, PKS 0252−71, PKS 1306−09, as discussed in Section 4.1). In these sources the derived systemic redshift was an average of the redshifts of the two components.

In addition to emission originating from the NLR, we have detected broad components to the permitted lines (due to the S/N of the data, often only detected in Hα), i.e. from the BLR, in three
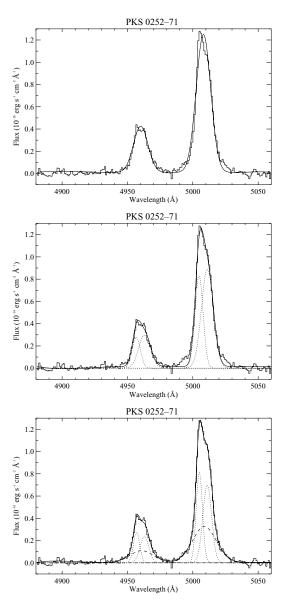
Figure 2. The effect of the overall fit to the [O III]λλ4959,5007 emission-line doublet in the nuclear aperture of PKS 0252−71 when fitting one (top), two (middle) and three (bottom) Gaussian components to each line in the doublet. In each plot, the overall profile (bold line) is overplotted on the extracted spectrum (faint line) and the dotted, dashed and dot–dashed lines highlight the relative positions and fluxes of the contributing components. It is clear that, in the nuclear aperture of PKS 0252−71, a minimum of three Gaussian components is required to model the emission lines well.

sources: 3C 268.3, 3C 277.1 and PKS 1549−79 (H06). 3C 277.1 is known to be a quasar and so the detection of a broad component to the permitted lines was not surprising. However, the detection of a broad component in Hα in 3C 268.3 has led to us reclassifying this radio source as a BLRG rather than an NLRG. The detection of broad Hα and Paα in PKS 1549−79 was reported in H06. The line data for the BLR components is presented in Table 4.

4.3 Single Gaussian modelling

Whilst multiple Gaussian modelling has worked well for the majority of sources in the sample, two GPS sources (PKS 1345+12 and

PKS 1934−46) were notable exceptions. In PKS 1345+12, a common narrow component was observed in all lines although different emission lines required different velocity widths and shifts for the broader components to provide good fits (H03). In PKS 1934−46, the situation is somewhat worse – it is less clear that a common narrow component exists for all lines when observed at this resolution and/or S/N.

For PKS 1345+12, H03 suggested a stratified ISM with three distinct regions, each responsible for the emission of one of the kinematic components. Hence, the different intermediate and broad components could be explained by gradients in ionization potential and/or critical density across the regions emitting the intermediate and broad components. Stratification of the NLR was suggested as the reason for correlations between emission-line FWHM (when fitting a single Gaussian) and ionization potential or critical density in Seyfert galaxies (de Robertis & Osterbrock 1984; de Robertis & Osterbrock 1986). This is consistent with models in which there is a continuous variation of density, ionization and velocity across a spatially unresolved inner NLR (INLR). This technique was applied to a sample of extended radio galaxies by Taylor (2004). In the latter work, no significant correlations were found in Cygnus A or in the sample of NLRGs, three out of the four BLRGs studied did show significant correlations with ionization potential and/or critical density, a feature expected for an INLR on a scale less than that of the central obscuring torus ($r < 100$ pc).

We have modelled all nuclear emission lines in all sources using single Gaussian free fits. No clear correlations were observed for the majority of the sources, including the BLRGs, in contrast to the results of Taylor (2004). Fig. 4 shows plots of the single Gaussian FWHM versus both critical density and ionization potential for the smaller sources in the sample: PKS 1345+12, PKS 1549−79 and PKS 1934−63. Whilst visual inspection of the plots suggests trends, particularly in critical density, Spearman rank analysis shows these visual trends to be insignificant.

The linewidths (FWHM) derived from the single Gaussian modelling can also be used to compare this sample of compact radio sources to other samples of radio sources presented in the literature. The measured single Gaussian FWHM of the nuclear [O III] lines for this sample are presented in Table 5 and are compared to a sample of extended radio sources in Section 5.

5 DISCUSSION

5.1 Extreme emission-line outflows

The nuclear emission lines in all of the compact radio sources in this sample are highly broadened, with complex emission-line profiles, and require multiple Gaussian components to model them. These components are often shifted significantly with respect to one another and are therefore likely to trace flows in the nuclear emission-line gas. However, in order to distinguish between inflows and outflows, it is necessary to accurately define the systemic velocity.

In Section 4.1, following a similar approach to that used for PKS 1345+12 (H03) and PKS 1549−79 (H06), we argued that the extended narrow component(s) represents the ambient, quiescent ISM in the galaxy halo. We are confident of this result in 12 of the 14 sources studied (see Section 4.1) – kinematically the narrow component is the least disturbed component and is typically the only extended component. In some of the sources in which H I absorption is detected, the velocity of the narrow component is also consistent with a deep, narrow component of H I which could be associated with a circumnuclear disc or torus (Morganti et al. 2001).
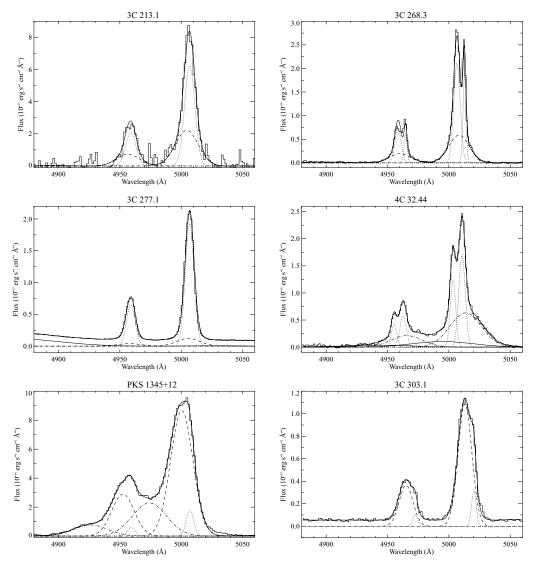
Figure 3. Models to the [O III]λλ4959,5007 emission-line doublet in the nuclear apertures of all 14 sources in the sample. The faint solid line represents the continuum subtracted spectrum and the bold solid line is the overall model fit to the doublet. The components are: narrow (dotted), intermediate (dashed), broad (dot–dashed) and very broad (dot–dot–dashed) for all sources except 3C 277.1 where the dot–dot–dashed line traces the BLR component of Hβ (see Section 3.3 for the kinematic definitions). All plots are on the same wavelength (i.e. velocity) scale to allow for comparisons between the outflows.

Previous studies have often struggled to determine the relationship between the H I, the optical kinematics and the systemic velocity (i.e. is the H I at rest, or tracing a flow of gas?) due to the inaccuracies in tying down the systemic velocities (see Morganti et al. 2001 for a discussion). In this paper, we have accurately established the systemic velocities in 12 out of 14 sources using detailed optical emission-line modelling and have compared them to the H I data available in the literature in Fig. 1 and Table 6.

H I absorption is detected in 10/14 sources. Comparing the optical and H I data, it is striking that the majority of absorption components are significantly blueshifted with respect to the optical systemic velocity, often by several hundreds of km s^{-1}, and represent outflows of neutral gas. Only three sources have H I components consistent with the optical systemic velocity (3C 213.1, 3C 268.3 and PKS 1345+12) which may be consistent with a circumnuclear disc or torus. However, in PKS 1345+12, the latest data show the component of H I at the systemic velocity is actually most likely associated with an off-nucleus cloud (Morganti et al. 2004). Unlike the optical outflows, both the narrower and broader line components have

significant blueshifts. Multiple H I components are observed in five sources. In PKS 1345+12, these are broadly consistent (velocity width and shift) with the optical components. Finally, two sources contain components consistent with infalling clouds (PKS 1934−63 and PKS 0023−26).

One of the key trends highlighted above (Section 4.2) is the detection of significantly shifted emission-line components observed in the majority of sources in the sample. These are predominantly *blueshifted*, with the broader components blueshifted by the largest amounts. Fig. 7 shows the distribution of shifts[7] for the sample. All sources except PKS 1306−09 – which has no 'broad' component,

---

[7] Note that for the sample described in this paper, the broadest (i.e. broadest NLR component) to systemic velocity shift is used rather than the broadest to narrow velocity shift. This is because several sources have multiple narrow components which are believed to trace rotation curves in the galaxy rest frame and using the systemic velocity is the most consistent method for all sources in the sample.
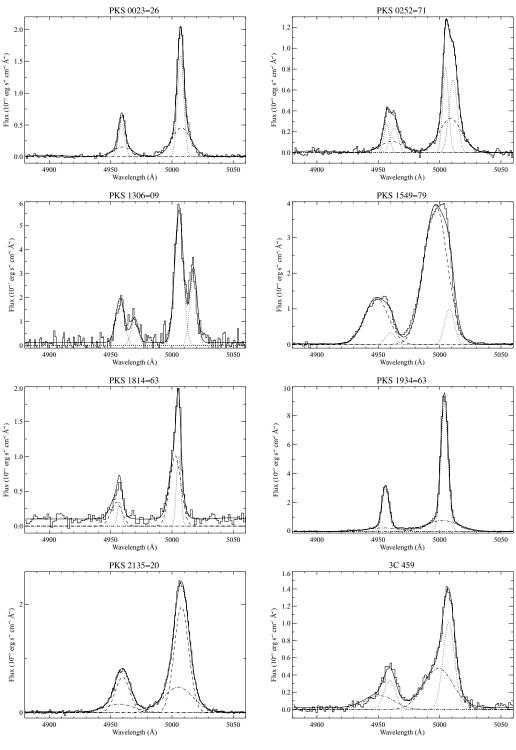
Figure 3 – *continued*

only two narrow components – are included in this plot and the shifts used are for the NLR components only.

For all but two sources (PKS 0023−26 and PKS 0252−71) the broad component is blueshifted with respect to the systemic velocity with velocities up to 2000 km s^{-1} although most sources occupy the range $-900 < v_{shift} < 100$ km s^{-1}. Fig. 7 further sub-divides the sample into the larger CSS sources and the smaller GPS sources. The effects of radio source size and orientation are discussed below.

The [O III] line emission is known to be resolved in three of the sources in this sample: 3C 268.3, 3C 277.1 and 3C 303.1. These sources have been imaged at high resolution with *HST* (de Vries et al. 1997, 1999; Axon et al. 2000) and O'Dea et al. (2002) have obtained corresponding *HST*/STIS spectroscopy of 3C 277.1 and 3C 303.1. For these sources, virtually all of the line emission detected by both de Vries et al. (1999) and Axon et al. (2000) lies within our slit. In our 2D spectra, we observe clear extended line emission in 3C

Table 4. Rest-frame emission-line modelling results. Columns are: (1) object name; (2) component following the definitions above: n (narrow; rn and bn denote the 'reddest' and 'bluest' component where two narrow components are detected), i (intermediate), b (broad), vb (very broad) and BLR (broad-line region component; i.e. a highly broadened component only observed in the permitted lines); (3 and 4) velocity width (FWHM) and error of each component; (5 and 6) velocity shift and error of the component from the systemic velocity. Note that the results for PKS 1345+12 and PKS 1934−63 are for [O III]. In sources for which free fitting gave two narrow components with different widths but the lines can also be modelled adequately by forcing the FWHM of the two narrow components to be equal, the FWHM of this alternative model for the narrow component is given and marked †.

Object		Velocity width (km s^{-1})	Δ (km s^{-1})	Velocity shift (km s^{-1})	Δ (km s^{-1})
(1)	(2)	(3)	(4)	(5)	(6)
3C 213.1	n	523	44	–	–
	i	1287	174	−142	65
3C 268.3	rn	309	12	–	–
	bn	unres	–	–	–
	i	1152	88	−121	22
	BLR	5664	525	−760	122
3C 277.1	n	462	6	+50	–
	i	1340	157	−79	36
	BLR	5177	185	335	31
4C 32.44	rn	316	6	176	8
	bn	242	6	−264	6
	b	1831	73	360	22
	vb	3548	380	−852	442
	n†	281	5		
PKS 1345+12	n	340	23	–	–
	i	1255	12	−402	9
	b	1944	65	−1980	36
3C 303.1	n	51	27		
	i	747	17	−438	20
PKS 0023−26	n	unres	–		
	i	1002	69	33	14
PKS 0252−71	rn†	335	30	–	–
	bn†	335	30	–	–
	i	1236	68	65	24
PKS 1306−09	rn	329	34	706	7
	bn	425	20	–	–
	n†	365	13		
PKS 1549−79	n	383	15	–	–
	i	1282	25	−679	20
PKS 1814−63	n	unres			
	i	569	35	−162	21
PKS 1943−63	n	unres			
	b	1785	103	−93	43
PKS 2135−20	i	762	15		
	b	1686	84	−157	29
3C 459	n	528	24	–	–
	b	1647	48	−497	49

268.3 and 3C 277.1 although the line emission imaged by *HST* lies within our defined nuclear aperture, within which no obvious spatial structure is resolved. The extended line emission that we detect will be presented in Holt et al. (in preparation) along with a discussion of extended apertures. It is difficult for us to compare our kinematic results to those of O'Dea et al. (2002) as whilst their spectra are of significantly higher spatial and spectral resolution compared to ours, from the figures in their paper, the lines are at much lower S/N than our spectra and they have, for the main part, modelled the

emission lines with single Gaussians. Depending on the dominance of different components, this can lead to erroneous line shifts (see e.g. H06). Comparing our single Gaussian modelling, we observe similar linewidths (FWHM ∼ 500 km s^{-1}) in 3C 277.1 but significantly higher widths in 3C 303.1 (FWHM ∼ 800 km s^{-1} compared to ∼500 km s^{-1} in O'Dea et al. 2002). Further, the resolved [O III] emission may account for the narrow line splitting in 3C 268.3.

From the results presented here, it is clear that, with the exception of PKS 0023−26, PKS 0252−71 and PKS 1306−09, all sources in the sample have evidence for fast, blueshifted flows in the circum-nuclear ISM. However, from the kinematical evidence alone it is impossible to distinguish between material in outflow on the side of the nucleus closest to the observer and material infalling on the far size of the nucleus. H03 argued that, for PKS 1345+12, as the reddening increased significantly with FWHM, the blueshifted components were likely to be consistent with material being observed on the observer's side of the nucleus and therefore tracing an outflow. We will discuss the issue of reddening in a future paper (Holt et al., in preparation).

5.2 The role of orientation

The original work on the compact flat spectrum radio source PKS 1549−79 by Tadhunter et al. (2001) suggested that the direction of jet propagation was oriented close to the observer's line of sight (LOS) as follows.

(i) PKS 1549−79 has a flat radio spectrum, often associated with radio-loud quasars whose axes are close to the observer's LOS.

(ii) PKS 1549−79 has core–jet radio morphology. As radio galaxies have two-sided radio jets, observing one-sided radio structure is usually interpreted as an orientation effect with the observer's LOS aligned close to the direction of jet propagation (see H06, fig. 10).[8]

Similarly, radio maps of PKS 1345+12 (e.g. Lister et al. 2003) show highly asymmetric radio jets, again suggesting the radio source is pointing close to the observer's LOS. This argument is supported by the detection of a broad (FWHM ∼ 2600 km s^{-1}) component Paα (Veilleux, Sanders & Kim 1997) and the detection of a point source component in high-resolution near-infrared images (Evans et al. 1999). However, this orientation is disputed by Lister, Kellermann & Pauliny-Toth (2002) and Lister et al. (2003) – see H03 for a discussion.

Interestingly, PKS 1345+12 and PKS 1549−79 contain two of the most extreme outflows in the sample discussed in this paper (∼2000 km s^{-1} and ∼680 km s^{-1}, respectively). Perhaps, then, the particular orientation of these objects with respect to our LOS is the reason why we observe such extreme kinematics in these sources. In contrast, for example, PKS 1934−63 has a weak core and is a symmetric double, as well as being one of the most compact sources in the sample, and has one of the smallest observed outflow velocities.

Due to the angular scales of the compact radio sources, compact flat spectrum radio cores for the sources in this sample are not generally detected, even with VLBI (e.g. Tzioumis et al. 2002) – the core is only detected in 5/14 sources. It is therefore not possible to determine the radio source orientation accurately for most of

---

[8] It should be noted that highly asymmetric radio structures are also consistent with jet–cloud interactions in a non-homogeneous ISM.
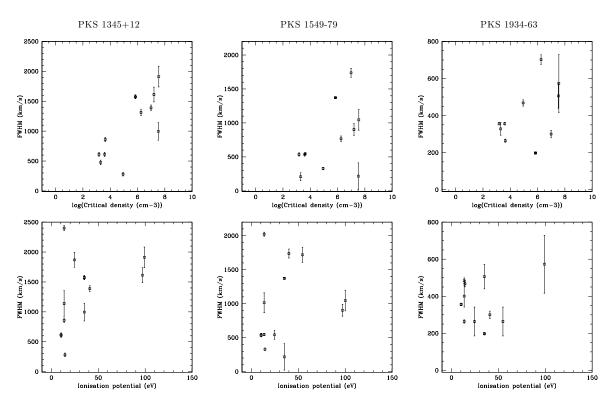
Figure 4. Correlation plots for the nuclear apertures of PKS 1345+12, PKS 1549−79 and PKS 1934−63. For each source the plots are: top: rest-frame FWHM (km s^{-1}) versus log(critical density cm^{-3}) and bottom: rest-frame FWHM (km s^{-1}) versus ionization potential (eV).

Table 5. Various emission-line parameters used in the statistical analysis. Columns are: (1) object; (2) heliocentric redshift of the systemic velocity; (3) maximum shift velocity taken as the shift between the broadest *NLR* component and the systemic velocity (km s^{-1}); 4 FWHM of the [O III]λ5007 line when fitting a single Gaussian (km s^{-1}); (5) the asymmetry index, AI$_{20}$ and (6) the kurtosis parameter, $R_{20/50}$. † *assumed* optical z. ⋆ Redshift derived from the stellar absorption lines.

Object	z	Max shift (km s^{-1})	[O III] FWHM (km s^{-1})	AI$_{20}$	$R_{20/50}$
(1)	(2)	(3)	(4)	(5)	(6)
3C 213.1	0.193 92 ± 0.000 04	−142	687 ± 22	−0.015 ± 0.002	1.65 ± 0.17
3C 268.3	0.371 71 ± 0.000 06	−760	668 ± 15	−0.20 ± 0.02	1.53 ± 0.15
3C 277.1	0.319 78 ± 0.000 08	−79	483 ± 4	−0.10 ± 0.01	1.79 ± 0.18
4C 32.44	0.368 01 ± 0.000 04	−852	986 ± 28	−0.054 ± 0.005	2.16 ± 0.22
PKS 1345+12	0.123 51 ± 0.000 08	−1980	1547 ± 32	0.55 ± 0.06	2.22 ± 0.22
3C 303.1	0.270 40 ± 0.000 06	−438	835 ± 8	−0.067 ± 0.007	1.45 ± 0.15
PKS 0023−26	0.321 62 ± 0.000 03	+33	262 ± 8	−0.046 ± 0.005	3.79 ± 0.38
PKS 0252−71	0.562 88 ± 0.000 09	+65	714 ± 9	−0.34 ± 0.03	1.68 ± 0.17
PKS 1306−09	0.466 85 ± 0.000 09	706^a	1009 ± 43	−0.46 ± 0.05	1.20 ± 0.12
PKS 1549−79	0.152 20 ± 0.000 03	−679	1372 ± 12	0.24 ± 0.02	1.43 ± 0.14
PKS 1814−63	0.064 66 ± 0.000 07†	−162	411 ± 17	0.28 ± 0.03	2.55 ± 0.26
PKS 1943−63	0.181 29 ± 0.000 08†	−93	198 ± 6	−0.001 ± 0.0001	1.69 ± 0.17
PKS 2135−20	0.636 34 ± 0.000 03†	−157	919 ± 7	0.033 ± 0.003	1.84 ± 0.18
	0.635 ± 0.004⋆				
3C 459	0.220 12 ± 0.000 03	−497	995 ± 33	0.25 ± 0.03	2.40 ± 0.24

^{a}The shift between the two detected narrow components.

the sample using the standard methods, for example, the R (core-dominance) parameter (e.g. Orr & Browne 1982; Giovannini et al. 2001), radio flux density comparison of the jet and counterjet (e.g. Giovannini et al. 2001), jet proper motion measurements (e.g. Giovannini et al. 2001) or jet motion modelling (e.g. Lister et al. 2003). Three sources have quoted orientation information in the literature: PKS 1549−79 ($R_{2.3\,GHz}$ = 1.310; Morganti et al. 2001), 3C

459 ($R_{4.8\,GHz}$ = 5.65; Morganti, Killeen & Tadhunter 1993; $R_{2.3\,GHz}$ = 0.394; Morganti et al. 2001) and PKS 1345+12 (jet motion modelling by Lister et al. 2003: 82° to LOS with opening angle of 46°, although this result is inconsistent with the arguments presented in H03).

Despite the lack of radio information to accurately determine the radio source orientations, it is still interesting to make a rough

Table 6. Summary of the H I data for the sample compiled from the literature. Columns are: (1) object, (2 and 3) H I velocity shift and error with respect to the optical systemic velocity derived in this paper where negative velocities imply blueshifted H I; (4 and 5) H I FWHM and estimated uncertainty; (6) optical depth; (7) H I column density derived assuming $T_{spin} = 100$ K and (8) references: v0: Véron-Cetty et al. (2000); m1: Morganti et al. (2001); m3: Morganti et al. (2003); v3: Vermeulen et al. (2003); g6: Gupta et al. (2006); H06: Holt et al. (2006); l6: Labiano et al. (2006); m: Morganti, private communication. ⋆ component of H I consistent with the optical systemic velocity. † Véron-Cetty et al. (2000) give e.g. FWZI and we have estimated the FWHM from their figures but also give their data here.

Object (1)	Velocity shift (km s^{-1}) (2)	Δ (km s^{-1}) (3)	FWHM (km s^{-1}) (4)	Δ (km s^{-1}) (5)	τ (10^{-2}) (6)	N(H I) (10^{20} cm^{-2}) (7)	Reference (8)
3C 213.1	−9⋆	7	115		0.05	0.11	v3
3C 268.3	−63	4	19		0.30	0.1	v3
	−152⋆	3	101		1.00	1.85	v3
	−116	10	67.1	6	2.5	3.2	l6
4C 32.44	−128	20	229		0.17	0.71	v3
PKS 1345+12	−15⋆		∼180		1	2	m3
	∼ −1600 to ∼175		∼1800^a		0.2	1	m3
	−360	1.7	23.5	3.9	0.0018^b	0.08	g6
	−393	0.8	22.8	1.8	0.0023^b	0.10	g6
	−450	0.4	129.9	0.7	0.0107^b	2.68	g6
PKS 0023−26	−64	40	39		0.20	0.14	v3
	45	6	126		0.93	2.14	v3
PKS 1306−09	−515 to −276		239^a		0.3		m
PKS 1549−79	−74	10	80		2	400	m1,H06
PKS 1814−63	−186		∼50		21.3	1700	m1
	0 to −281		∼280^a		0.8	2000	m1
	−192†	2	62†		21.7	9	v0†
	† ∼ −370 to ∼0		†372^a				
PKS 1934−63	389	2	20		0.22	0.06	v0
3C 459	−398	9	400		0.8	270	m1
	−241	10	130		0.31	0.72	v3
	−431	27	71	34	0.0012^b	0.17	g6
	−344	6	121	11	0.0034^b	0.8	g6
	−186	31	164	63	0.0012^b	0.38	g6

^{a}Full width at zero intensity (FWZI) of the broad, shallow absorption. ^{b}Quoted fractional absorption.

estimate of the importance of orientation with respect to the observed outflow velocities. For the remainder of the sample, we have therefore adopted the rather crude approach of comparing the relative extents of the radio jets on either side of the nuclei in the radio maps. Assuming both jets are generated by the same central source, if they expand through empty space they should have similar intrinsic extents on either side of the core and any observed differences will be due to orientation effects. It should be noted that, should the jets expand through a dense ISM, interactions between the radio source and this ISM could significantly alter the path of at least one of the jets. Hence, a highly asymmetric ISM can alter the relative extents of the jets and mimic the effects of orientation with respect to the observer and these results should therefore be used with caution. However, Best et al. (1995) studied the angular asymmetries in a sample of extended Fanaroff–Riley type II 3CR sources and found the distribution of asymmetry angles to be consistent with the predictions of unified schemes.

We have therefore classified the sources into three broad categories.

(i) Close to the LOS: All sources with an obvious core–jet and a large core/extended radio flux ratio e.g. PKS 1549−79, PKS 1345+12 and 3C 303.1.

(ii) Close to the plane of the sky: Symmetric radio morphology (e.g. similar jet extents and/or fluxes): e.g. PKS 1934−62, PKS 0252−71 and PKS 0023−26.

(iii) Intermediate: Sources not consistent with the other two categories.

Fig. 5 shows the grouping with respect to the largest outflow velocity.

Despite the crudeness of the method, the data suggest that the orientation of the radio source to the observer's LOS/the asymmetry of the radio morphology may be an important factor in determining the maximum outflow velocity observed. Sources with jets most likely pointing towards us contain the most extreme outflow velocities, and sources likely to be close the plane of the sky exhibit the least evidence for fast outflows in the NLR. Only two sources in the sample appear to be 'misfits' in this classification scheme – 3C 277.1 and 4C 32.44. This is most likely due to both the oversimplification of the method and inherent scatter in the data. Note also, whilst the flat spectrum core appears strong in the radio map of 3C 277.1 and we observe strong optical signatures of the quasar in our optical spectra (broad permitted lines and a strong blue power-law continuum), the radio emission is resolved into two distinct lobes which suggest the radio axis is not closely aligned with our LOS. We have therefore placed 3C 277.1 in the 'intermediate' category.

Such a strong trend in orientation–outflow velocity has been suggested for other classes of AGN. The most extreme outflows observed in any type of AGN are those in BAL quasars. Whilst the BAL outflows are on a different scale to those observed in compact radio sources (on the scale of the BLR rather than the NLR), it has been suggested that the extreme velocities observed may
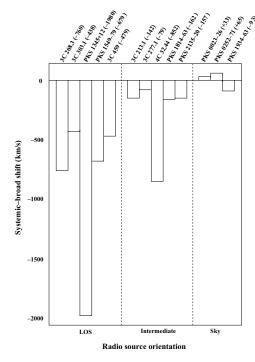
Figure 5. Histogram showing the putative orientation of the sources with respect to their outflowing velocities.

be partly due to an orientation effect (e.g. Weymann et al. 1991; Elvis 2000).

5.3 Outflow driving mechanism

It is clear that extreme emission-line kinematics exist in all of the compact radio sources in this sample. The emission-line flows are likely to trace outflows in the emission-line gas, similar to the results presented for PKS 1345+12 (reddening; H03) and PKS 1549−79 (source orientation; H06).

If compact radio sources are truly young AGN in which the outflows have not yet swept aside the natal cocoon, then because of the large gas and dust concentrations in the central regions, the effects of *all* types of outflow (quasar winds, jets, starburst superwinds) are likely to be more visible as there is more warm/cool gas around for the winds and/or jets to interact with. Whilst jet–cloud interactions are expected to produce extreme kinematics, all of these scenarios can potentially explain broad linewidths and large velocity shifts and so, from the kinematical evidence alone, it is not possible to distinguish between the different outflow driving mechanisms.

Some of the best evidence for jet-driven outflows is provided by the co-alignment and similar scales of the radio source and the optical emission-line structures. More than 30 CSS sources have been observed with *HST* in both broad- and narrow-bands (to isolate [O II] and/or [O III] emission) by de Vries et al. (1997, 1999) and Axon et al. (2000). The de Vries et al. samples include 3C 213.1, 3C 268.3, 3C 277.1 and 3C 303.1 and the Axon et al. sample includes 3C 268.3, 3C 277.1, 3C 303.1 and PKS 1345+12. These imaging studies reveal that the optical and radio emission are both

(i) on similar scales (30–90 per cent of the optical line emission is concentrated within a few kpc and the radio sources are either completely embedded within this optical line emitting gas or extend just beyond it; Axon et al. (2000) sample) and

(ii) strongly aligned (typically $\lesssim 10°$ in all sources, including the sources also found in our sample, in which the data could be accurately registered in the de Vries et al. sample, and in 6/11 sources in the Axon et al. sample, often elongated into jet-like structures).

The radio–optical alignment is also observed across the entire redshift range probed by these samples ($0.1 \lesssim z \lesssim 1.5$), rather than confined to higher redshifts as in more extended radio sources ($z \gtrsim 0.6$; e.g. McCarthy et al. 1987; de Koff et al. 1996). Such close association between the optical emission-line gas and the radio source suggest that the radio source is strongly interacting with the ambient medium as it expands through it (O'Dea et al. 2002). Follow-up *HST*/STIS spectroscopy of three CSS sources with resolved [O III] line emission (including 3C 277.1 and 3C 303.1) provides further evidence that the outflows are likely to be driven by the expanding radio jets; the emission lines have complex, broad profiles (FWHM $\sim 500\,\mathrm{km\,s^{-1}}$) which are offset with respect to the systemic velocity by 300–500 $\mathrm{km\,s^{-1}}$ in the region(s) of the radio hotspots (O'Dea et al. 2002) and the line ratios are consistent with a mixture of fast shocks (500–1000 $\mathrm{km\,s^{-1}}$) and photoionization/precursor (Labiano et al. 2005).

Finally, PKS 1345+12 and PKS 1549−79 were recently observed at higher resolution with *HST*/ACS (Batcheldor et al. 2007). In these sources, the optical line emission is clearly concentrated in the central regions, ruling out galaxy wide starbursts as the dominant outflow driving mechanism. Further, the radio emission in both sources is on similar scales to the optical line emission. However, the region of line emitting gas is only marginally resolved and, whilst there is a suggestion that the isophotes may be elongated in the direction of the radio axis, this evidence is far from conclusive.

Despite the strong evidence for radio/optical alignments and the cospatial scales of the optical and radio emission, we find no evidence for anticorrelations between the emission linewidths and the ionization potential (Fig. 4) that are a clear signature of shocks in some extended radio sources. Hence, to confidently distinguish between the different ionization mechanisms, it is necessary to combine the kinematical and imaging data with a detailed study of the line ratios (Holt et al., in preparation).

5.4 Are the kinematics in compact radio sources more extreme than in extended radio sources?

As discussed in Section 1, previous data have suggested that the kinematical properties of the *nuclear* emission-line gas are different in compact radio sources compared to more extended radio sources. For example, comparison of the emission-line profiles in samples of compact (e.g. Gelderman & Whittle 1994) and extended (e.g. Brotherton 1996) radio sources in the literature suggest that the line profiles of the compact radio sources are often broader and more asymmetric. However, to date, no attempt has been made to properly quantify the differences between the emission-line profiles of compact and extended radio sources.

Many of the spectra in the literature are not of sufficient S/N and/or resolution to model the emission-line profiles in detail and so we have used three line profile parameters on the strong [O III]λ5007 line to compare our sample to the data in the literature, for example, (i) the linewidth (FWHM) derived from single Gaussian modelling; (ii) the asymmetry index, AI_{20} and (iii) the kurtosis parameter, $R_{20/50}$. The latter two are defined in Heckman et al. (1981). All the results for our sample are presented in Table 5. As our sample of compact radio sources is small, we have formed a larger sample including data from the literature (see Table 8). Our comparison sample of extended radio
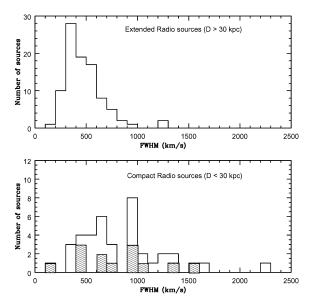
Figure 6. Histograms showing the distribution in observed optical emission-line FWHM of [O III] in samples of extended ($D > 30$ kpc; from Heckman et al. 1984 and Brotherton 1996) and compact ($D < 30$ kpc; this sample plus sources from Gelderman & Whittle 1994, four sources from the sample of Hirst, Jackson & Rawlings (2003) and PKS 1718−49 from Fosbury et al. 1977). The shaded part of the bottom plot highlights the sources from this sample.

Figure 7. Histograms showing the maximum nuclear outflow velocity for this sample of compact radio sources (bottom) and a comparison sample of extended radio sources taken from Taylor (2004). Note, for the extended sources the shift plotted is broadest–narrowest component whilst for the compact sources, the shift between the broadest systemic velocity is used as in a number of sources, two narrow components are observed (see Section 4.1). For the compact radio sources, the plot is further divided by scale – CSS, GPS and 'other' comprising compact core and compact flat spectrum radio sources. For the extended sources, the sample is divided into BLRG and NLRG. All shifts are derived from the nuclear apertures only.

sources for these three parameters comprises all radio-loud objects in the samples of Heckman, Miley & Green (1984) and Brotherton (1996) (see Table 7). The latter sample comprises solely quasars whereas the sample of Heckman et al. (1984) includes both radio galaxies and quasars.

Fig. 6 shows that the distribution of FWHM of [O III]λ5007 is markedly different for the compact and extended radio source samples. For the extended sources, the distribution peaks at $\sim$200–300 km s^{-1} which is consistent with gravitational motions in an elliptical galaxy (Tadhunter et al. 1989). However, more extreme kinematics are observed in the sample of compact radio sources – the spread is larger and it peaks at FWHM $\sim$ 1000 km s^{-1} – velocities which are too large to be explained by gravitational motions unless the gas was located close to the central black hole (i.e. in the BLR or an INLR). A one-tailed Kolmogorov–Smirnov (KS) test shows the distributions are different at the 99.9 per cent confidence level.[9] Whilst this effect might be due, in part, to orientation effects in both compact radio sources (see Fig. 5) and/or foreshortening of larger radio sources, it has been argued that the majority of CSS sources cannot be larger radio sources foreshortened by projection effects (Fanti et al. 1990).

Whilst the linewidths show a clear difference between the compact and extended sources, a KS test shows that neither the asymmetry index nor the kurtosis parameters are significantly different. Whilst we may initially expect the broad, blueshifted components to give highly asymmetric line profiles, examination of Fig. 3 shows in many sources, either the peak flux of the broadest components is often below the 20 per cent flux level (i.e. asymmetries would only be evident in parameters using e.g. the 10 per cent flux level
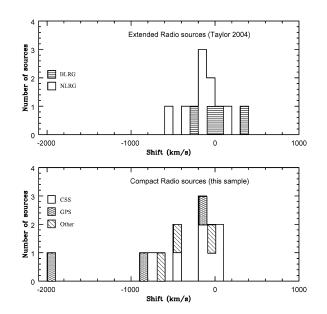
as in PKS 1345+12), or the emission lines appear symmetric although the dominant component may be highly shifted (e.g. PKS 1549−79).

In addition to the linewidths/profiles comparison to older data in the literature, we have compared our sample to a recent study of a sample of extended 3C radio sources taken with similar observational set-up (Taylor 2004) enabling comparisons between, for example, the shifts between the different components of a line (see Table 7). A histogram of the broadest narrow velocity shifts for both samples in shown in Fig. 7. The distributions are markedly different (99.9 per cent: KS test) with the compact radio sources spanning a much larger range in velocity (out to $\sim$2000 km s^{-1} compared to $\sim$600 km s^{-1}). It is interesting to note that this trend of more extreme velocities in smaller sources is also evident within the sample of compact radio sources, with the two most extreme velocities being detected in smaller GPS sources (PKS 1345+12 and 4C 32.44). Indeed, all but one of the most extreme velocities ($v > 500$ km s^{-1}) are detected in sources with projected linear size $D < 1$ kpc whilst the cluster of sources in the low outflow velocity region ($-100 < v_{shift} < 100$ km s^{-1}) are predominantly the larger CSS sources (Fig. 7 and Table 8). Such velocity evolution with source size is consistent with the idea that compact radio sources are young, starting as GPS sources and expanding to become CSS then extended radio sources.

Whilst the nuclear regions of extended radio sources appear to be less extreme than in more compact radio sources, extreme velocities ($v \gtrsim 1000$ km s^{-1}; e.g. Solórzano-Iñarrea, Tadhunter & Axon 2001) are commonly observed in extended radio sources, but in the *extended* emission-line regions (EELRs). EELRs are typically on similar scales as, and are aligned with, the radio axis and are therefore associated with jet–cloud interactions. Hence, in extended

---

[9] Whilst the KS test reveals a strong trend, the reader should also remember that the various samples have different selection criteria which may affect the test to some degree.

Table 7. Parameters for the comparison samples used in both this paper and in Holt et al. (in preparation). Columns are: (1) sample name; (2) redshift range; (3) radio power range at 5 GHz; (4) number of sources used; (5) completeness of the sample. † see Section 2 for details. Note, for sources which are included in more than one sample, data are included only once and are taken from the sample with the highest quality data. ⋆ This comparison sample is only used in Holt et al. (in preparation).

Sample	z	Radio power $\log P_{5GHz}$ (W Hz^{-1})	N	Completeness
(1)	(2)	(3)	(4)	(5)
Compact radio sources				
This paper	<0.7	26–28	14	Complete†
Gelderman & Whittle (1994)	<0.9	22–29	16	Not complete
Hirst et al. (2003)	0.5–3.6	>26.5^a	9	Complete
PKS 1151−34	0.258	26.8		
PKS 1718−643	0.014	24.3		
Extended radio sources				
2 Jy	<0.7	25–29	36	Complete ⋆
Radio-loud objects from Heckman et al. (1984)	<0.7	>24.5^b	45	Not complete
Radio-loud objects from Brotherton (1996)	<0.95	–^{c}	60	Not complete
Taylor (2004)	<0.2	26–29	12	Complete

^{a}Radio power range at 5 GHz except at 178 MHz. ^{b}Radio power range at 5 GHz except at 1.4 GHz. ^{c}No radio data was given for this sample.

radio sources, the regions emitting the broader components are often significantly displaced from the nuclear aperture, coincident with the radio emission.

With this in mind, it is not surprising that extreme kinematics are observed in the *nuclear* apertures of compact radio sources. Compact radio sources are on the scale of the host galaxy (<15 kpc), often contained within the nuclear regions ($\lesssim$1 kpc), and so the signatures of interactions between the radio jets and the ISM will occur in the circumnuclear regions. Indeed, it is in the nuclear apertures of compact radio sources that we observe both broad, blueshifted components, which are generally spatially unresolved, as well as any quiescent components similar to those observed in the nuclear regions of extended radio sources. The consistency between the spatial scales of the ELRs and the radio emission has been confirmed in six sources in our sample (3C 213.1, 3C 268.3, 3C 277.1, 3C 303.1, PKS 1345+12 and PKS 1549−79) using *HST* broad- and narrow-band imaging (de Vries et al. 1997; Axon et al. 2000; Batcheldor et al. 2007). Hence, whilst the kinematics observed in the nuclear regions of compact radio sources are significantly different to those observed in the nuclei of more extended radio sources, they are entirely consistent with compact radio sources being a young, small-scale version of the jet–cloud interactions observed in the extended sources with aligned radio and optical emission.

Table 8. Comparison of the maximum outflow velocity with the largest projected linear size of the sources in this sample.

$D < 1$ kpc		$D > 1$ kpc	
4C 32.44	(−852)	3C 213.1	(−142)
PKS 1345+12	(−1980)	3C 268.3	(−760)
PKS 1549−79	(−679)	3C 277.1	(−79)
PKS 1814−63	(−162)	3C 303.1	(−438)
3C 459^a	(−497)	PKS 0023−26	(+33)
		PKS 0252−71	(+65)
		PKS 1306−09	(0)
		PKS 1934−63	(−93)
		PKS 2135−20	(−157)

^{a}Compact core.

6 SUMMARY, CONCLUSIONS AND FUTURE WORK

It is clear that all compact radio sources show evidence for disturbed kinematics, with large linewidths and shifts with respect to the galaxy rest frame in the optical emission lines. The main conclusions of this paper are as follows.

(i) The extended emission-line halo: For the majority of sources (12/14), we were able to determine the systemic velocity with confidence. For consistency, all techniques focused on the extended narrow component emission. In two sources, a smooth 'rotation curve' was observed, but in most sources, the extended narrow component emission was either not settled, as in PKS 1345+12, or split into two narrow components, assumed to represent a rotation curve in which the central regions were unresolved although this may also be a signature of bipolar outflows.

(ii) Extreme emission-line outflows: All but three sources show evidence for outflows in the circumnuclear ISM. The most extreme outflow is in the GPS source PKS 1345+12 ($\sim$2000 km s^{-1}). Interestingly, the second most extreme outflow was observed in another GPS source, 4C 32.44. As well as radio source size (CSS or GPS), the orientation of the radio source to the observer's LOS may also be important, with higher outflow velocities observed in sources pointing towards the observer.

(iii) Blueshifted H I: H I absorption is detected in 10/14 sources, with multiple components observed in five sources. The majority of H I components (narrow and broad) are significantly blueshifted with respect to the systemic velocity and trace outflows in the neutral gas. In PKS 1345+12 the outflowing H I components are broadly consistent with the emission-line components. In only two sources (PKS 0023−26 and PKS 1934−63) is the H I redshifted, consistent with infalling gas.

(iv) Kinematical evidence for shocks: As well as the extreme line splitting/outflows, the emission-line components are also highly broadened. Again, the two most extreme FWHM in the NLR gas are observed in GPS sources: PKS 1345+12 ($\sim$2000 km s^{-1}) and 4C 32.44 ($\sim$3500 km s^{-1}). Highly broadened components are almost exclusively confined to the nuclear apertures and therefore on the scale of the radio source. Higher resolution *HST* studies have

resolved the [O III] emission-line gas in several sources in this sample, revealing that the emission-line gas is both on the same scale as, and is strongly aligned with, the radio source. This is consistent with observations of high-redshift extended radio sources in which the broadest components are observed in regions coincident with the radio emission (e.g. Solórzano-Iñarrea et al. 2001). The suggested importance of orientation on the observed outflow velocity also suggests the acceleration is confined to a spatially small region (i.e. coincident with radio jets) rather than occurring across the entire nuclear region (i.e. due to a quasar or starburst wind).

(v) Smaller source – more extreme kinematics: These results provide further evidence that the radio source size is also important in determining the outflow velocity and the dominance of shocks. Shocks, and the kinematics associated with them, are predominantly confined to smaller *extended* sources ($D \lesssim 120$ kpc: Best, Röttgering & Longair 2000). The statistical tests presented in this paper show that the nuclear kinematics, in particular the emission-line shifts, are more extreme in compact radio sources than in the nuclear regions of their extended counterparts at the 99.9 per cent confidence level. Similarly, the most extreme outflows in the compact radio sources occur in sources with the smallest projected linear sizes, generally with $D < 1$ kpc, the GPS sources. Whilst this effect might be due, in part, to foreshortening, it has been argued that the majority of CSS sources cannot be larger radio sources foreshortened by projection effects (Fanti et al. 1990).

ACKNOWLEDGMENTS

REFERENCES

Axon D. J., Capetti A., Fanti R., Morganti R., Robinson A., Spencer R., 2000, AJ, 120, 2284
Balsara D. S., Krolick J. H., 1993, ApJ, 402, 109
Batcheldor D., Tadhunter C. N., Holt J., Morganti R., O'Dea C. P., Axon D. J., Koekemoer A., 2007, ApJ, 661, 70
Best P. N., Bailer D. M., Longair M. S., Riley J. M., 1995, MNRAS, 275, 1171
Best P. N., Röttgering H. J. A., Longair M. S., 2000, MNRAS, 311, 1
Best P. N., Kaiser C. R., Keckman T. M., Kauffmann G., 2006, MNRAS, 368, 67
Bicknell G., Dopita M. A., O'Dea C. P., 1997, ApJ, 485, 112
Bower R. G., Benson A. J., Malbon R., Helly J. C., Frenk C. S., Baugh C. M., Cole S., Lacey C. G., 2006, MNRAS, 370, 645
Brotherton M. S., 1996, ApJS, 102, 1
Bruzual A. G., Charlot S., 1993, ApJ, 405, 538
Croton D. J. et al., 2006, MNRAS, 365, 11
de Koff S., Baum S. A., Sparks W. B., Biretta J., Golombek D., Macchetto F., McCarthy P., Miley G. K., 1996, ApJS, 107, 621
de Robertis M. M., Osterbrock D. E., 1984, ApJ, 286, 171
de Robertis M. M., Osterbrock D. E., 1986, ApJ, 301, 727
de Vries W. H. et al., 1997, ApJ, 110, 191

de Vries W. H., O'Dea C. P., Baum S. A., Barthel P. D., 1999, ApJS, 526, 27
Di Matteo T., Springel V., Hernquist T., 2005, Nat, 433, 604
Dickson R. D., Tadhunter C. N., Shaw M., Clark N., Morganti R., 1995, MNRAS, 273, 29
Elvis M., 2000, ApJ, 545, 63
Evans A. S., Kim D. C., Mazzarella J. M., Scoville N. Z., Sanders D. B., 1999, ApJ, 521, L107
Fabian A. C., 1999, MNRAS, 308, L39
Fanti C., Fanti R., Schilizzi R. T., Spencer R. E., Stanghellini C., 1995, A&A, 302, 317
Fanti R., Fanti C., Schilizzi R. T., Spencer R. E., Rendong N., Parma P., van Breugel W. J. M., Venturi T., 1990, A&A, 231, 333
Ferrarese L., Merritt D., 2000, ApJ, 539, 9
Fosbury R. A. E., Mebold U., Goss W. M., van Woerden H., 1977, MNRAS, 179, 89
Gebhardt K. et al., 2000, ApJ, 539, 13
Gelderman R., Whittle M., 1994, ApJS, 91, 491
Giovannini G., Cotton W. D., Feretti L., Lara L., Venturi T., 2001, ApJ, 552, 508
Gupta N., Salter C. J., Saikia D. J., Ghosh T., Jeyakumar S., 2006, MNRAS, 373, 972
Heckman T. M., Miley G. K., van Breugel W. J. M., Butcher H. R., 1981, ApJ, 247, 403
Heckman T. M., Miley G. K., Green R. F., 1984, ApJ, 281, 525
Heckman T. M., Smith E. P., Baum S. A., van Breugel W. J. M., Miley G. K., Illingworth G. D., Bothun G. D., Balick B., 1986, ApJ, 311, 526
Hirst P., Jackson N., Rawlings S., 2003, MNRAS, 346, 1009
Holt J., Tadhunter C. N., Morganti R., 2003, MNRAS, 342, 227 (H03)
Holt J., Tadhunter C. N., Morganti R., Bellamy M. J., González Delgado R. M., Tzioumis A., Inskip K. J., 2006, MNRAS, 370, 1633 (H06)
Holt J., Tadhunter C. N., González Delgado R. M., Inskip K. J., Rodriguez Zaurin J., Emonts B. H. C., Morganti R., Wills K. A., 2007, MNRAS, 381, 611
Hopkins P. F., Hernquist L., Cox T. J., Di Matteo T., Martini P., Robertson B., Springel V., 2005, ApJ, 630, 705
Kellermann K. I., Pauliny-Toth I. I. K., Williams P. J. S., 1969, ApJ, 157, 1
Labiano A. et al., 2005, A&A, 436, 493
Labiano A., Vermeulen R. C., Barthel P. D., O'Dea C. P., Gallimore J. F., Baum S., de Vries W., 2006, A&A, 447, 481
Lister M. L., Kellermann K. I., Pauliny-Toth I. I. K., 2002, in Ros E., Porcas R. W., Zensus J. A., eds, Proceedings of the 6th European VLBI Network Symposium, Bonn, Germany. Max-Planck Institut für Radioastronomie, Bonn, p. 135
Lister M. L., Kellermann K. I., Vermeulen R. C., Cohen M. H., Zensus J. A., Ros E., 2003, ApJ, 584, 135
Marconi A., Hunt L. K., 2003, ApJ, 589, L21
McCarthy P. J., van Breugel W., Spinrad H., Djorgovski S., 1987, ApJ, 321, 29
Morganti R., Killeen N., Tadhunter C. N., 1993, MNRAS, 263, 1023
Morganti R., Oosterloo T. A., Tadhunter C. N., van Moorsel G., Killeen N., Wills K. A., 2001, MNRAS, 323, 331
Morganti R., Tadhunter C. N., Oosterloo T. A., Holt J., Tzioumis A., Wills K., 2003, Publ. Astron. Soc. Aust., 20, 129
Morganti R., Oosterloo T. A., Tadhunter C. N., Vermeulen R., Pihlström Y. M., van Moorsel G., Wills K. A., 2004, A&A, 424, 119
Murgia M., Fanti C., Fanti R., Gregorini L., Klein U., Mack K. H., Vigotti M., 1999, A&A, 345, 769
O'Dea C. P., 1998, PASP, 110, 493
O'Dea C. P. et al., 2002, AJ, 123, 2333
Orr M. J. L., Browne I. W. A., 1982, MNMRAS, 200, 1067
Osterbrock D. E., 1989, Astrophysics of Gaseous Nebulae and Active Galactic Nuclei. University Science Books, California, p. 61
Osterbrock D. E., Fulbright J. P., Keane M. J., Trager S. C., 1996, PASP, 108, 277
Owsianik I., Conway J. E., Polatidis A. G., 1998, A&A, 336, L37
Robinson T. G., 2001, PhD thesis, Univ. Sheffield

Rodriguez Zaurin J., Holt J., Tadhunter C. N., Gonzalez Delgado R. M., 2008, MNRAS, 375, 1133

Schlegel D. J., Finkbeiner D. P., Davis M., 1998, ApJ, 500, 525

Seaton M. J., 1979, MNRAS, 187, 73P

Silk J., Rees M. J., 1998, A&A, 331, L1

Solórzano-Iñarrea C., Tadhunter C. N., Axon D. J., 2001, MNRAS, 323, 965

Stanghellini C., Baum S. A., O'Dea C. P., Morris G. B., 1990, A&A, 233, 379

Stanghellini C., Dallacasa D., O'Dea C. P., Baum S. A., Fanti R., Fanti C., 1996, in Snellen I. A. G., Schilizzi R. T., Röttgering H. J. A., Bremer M. N., eds, Proceedings of the Second Workshop on Gigahertz Peaked-Spectrum and Compact Steep Spectrum Radio Sources, Leiden, Leiden Observatory, Leiden. p. 4

Tadhunter C. N., Fosbury R. A. E., Quinn P. J., 1989, MNRAS, 24, 225

Tadhunter C. N., Morganti R., di Serego Alighieri S., Fosbury R. A. E., Danziger I. J., 1993, MNRAS, 263, 999

Tadhunter C. N., Wills K., Morganti R., Oosterloo T., Dickson R., 2001, MNRAS, 327, 227

Tadhunter C. N., Robinson T. G., González Delgado R. M., Wills K., Morganti R., 2005, MNRAS, 356, 480

Taylor M. D., 2004, PhD thesis, Univ. Sheffield

Taylor M. D., Tadhunter C. N., Robinson T. G., 2003, MNRAS, 342, 995

Tremaine S. et al., 2002, ApJ, 574, 740

Tschager W., Schillizi R. T., Röttgering H. J. A., Snellen I. A. G., Miley G. K., 2000, A&A, 360, 887

Tzioumis A. et al., 2002, A&A, 392, 841

van Breugel W. J. M., 1984, in Fanti R., Kellerman K. I., Setti G., eds, Proc. IAU Symp. 110, VLBI and Compact Radio Sources. Reidel, Dordrecht, p. 59

Veilleux S., Sanders D. B., Kim D.-C., 1997, ApJ, 484, 92

Vermeulen R. C. et al., 2003, A&A, 404, 861

Véron-Cetty M.-P., Woltjer L., Stavely-Smith L., Ekers R. D., 2000, A&A, 362, 426

Villar-Martín M., Tadhunter C. N., Morganti R., Axon D. J., Koekemoer A., 1999, MNRAS, 307, 24

Wall J., Peacock J., 1985, MNRAS, 216, 173

Weymann R. J., Morris S. L., Foltz C. B., Hewett P. C., 1991, ApJ, 373, 23

Wills K. A., Tadhunter C. N., Holt J., Gónzalez Delgado R., Inskip K. J., Rodríguez Zaurín J., Morganti R., 2008, MNRAS, 385, 136

This paper has been typeset from a TEX/LATEX file prepared by the author.